

Asymmetrical anchor way of manganese atoms on carbon domain edge for enhanced oxygen reduction reaction

Meiping Li^{a,b}, Zhufeng Hou^d, Xiaodong Li^b, Xiangyao Gu^{b,c}, Xingru Yan^{b,c}, Qing Lv^{a,*}, Changshui Huang^{a,b,c,*}

^a Shandong Provincial Key Laboratory for Science of Material Creation and Energy Conversion, School of Chemistry and Chemical Engineering, Shandong University, Jinan 250100, PR China

^b Beijing National Laboratory for Molecular Sciences (BNLMS), CAS Research/Education Center for Excellence in Molecular Sciences, Institute of Chemistry Chinese Academy of Sciences, Beijing 100190, PR China

^c University of Chinese Academy of Sciences, Beijing 100049, PR China

^d State Key Laboratory of Structural Chemistry, Fujian Institute of Research on the Structure of Matter, Chinese Academy of Sciences, Fuzhou 350002, PR China



ARTICLE INFO

Keywords:

Oxygen reduction reaction
Single-atom catalyst
Graphdiyne
Zinc-air battery

ABSTRACT

Single atomic catalysts (SACs), especially the catalysts featured by well-developed M-N₄ moieties, show excellent catalytic activity and spark enormous attention. However, the highly symmetric active sites may result in some degenerate electronic states for the d orbitals of the center metal atom, which suffer from the unsatisfactory adsorption-desorption behaviors during reaction. Herein, we develop an asymmetric anchor site by two types of nitrogen (sp-N and pyridinic N) created in the inherent edge-rich carbon domain of hydrogen-substituted graphdiyne (HsGDY), where atomic catalyst like manganese atoms can be asymmetrically anchored on the one side of hexagon carbon rings. The abundant elegant hexagon carbon rings on HsGDY not only facilitate the creation of edge sites, but also provide available space for the coordination of terminal ligands (OH) with Mn atoms. The as-synthesized Mn-N-HsGDY exhibits excellent ORR activity and an impressive long-term cyclability for over 3800 cycles in a rechargeable Zn-air battery.

1. Introduction

Single-atom catalysts (SACs) have emerged as a booming field due to their impressive catalytic performance comparable to that of precious metal catalysts [1–8]. Among them, single-atom metal-nitrogen-carbon (M-N-C) materials, especially the materials featuring with M-N₄ moieties exhibit high catalytic activity in various reactions (such as oxygen reduction reaction (ORR) [9–12], hydrogen evolution reaction (HER) [13] and CO₂ reduction reaction (CO₂RR) [14,15]). Nevertheless, recent studies have demonstrated that symmetric planar structure of well-defined M-N₄ is endowed with degenerate electronic states (for example, the dxz and dyz orbitals of the center M atom), which results in the discontented adsorption energies and limited electrocatalytic activity [16–19]. To improve the catalytic activity, some heteroatoms, such as P, S, Cl and OH, are introduced into the M-N-C catalysts to break the symmetry of active center and the degenerate electronic states [20–23]. Commonly, most of those sites are formed based on

graphene-like supports [2,6]. Due to the high atomic density of the benzene rings, those carbon supports are not easy to form proper defects suitable for the coordination of metal atoms with large-diameter heteroatoms. Besides, excessive defects will reduce the electroconductivity of the catalysts [24]. It has also been demonstrated that the edges of carbon matrix are conducive to stabilizing atomic metals to form edge active sites that exhibit superior activity than the in-plane ones [25–28], while edge carbon atoms are in the minority for graphene. Therefore, it is of great significance to explore an edge-rich carbon substrate that can facilitate the creation of edge sites without forming defects.

In our previous work, we have reported the using of molecular pore of hydrogen-substituted graphdiyne (HsGDY) as edge site to doping nitrogen (N) atoms [29–32]. For HsGDY, three of the carbon atoms on a benzene ring are bonded to diacetylene chain (-C≡C-C≡C-), whereas the other three are linked to hydrogen atoms, forming a conjugated structure with abundant molecular pores. The existence of sp²-C and sp-C in HsGDY leads to the formation of pyridine N (referred as py-N) and sp-N

* Corresponding authors at: Shandong Provincial Key Laboratory for Science of Material Creation and Energy Conversion, School of Chemistry and Chemical Engineering, Shandong University, Jinan 250100, PR China.

E-mail addresses: lvqing@sdu.edu.cn (Q. Lv), huangcs@iccas.ac.cn (C. Huang).

when nitrogen atoms are introduced [31–33], which are different from the types of nitrogen formed in graphene-like substrates. Experiments and calculations have demonstrated that the sp-N possesses more negative charge density than other hybridization-types of nitrogen [33–37]. Thus, when sp-N and py-N are simultaneously coordinated with metal atoms, asymmetric sites are created directly. Moreover, abundant inherent edge-rich carbon domain and elegant molecular pores of HsGDY facilitate the formation of edge sites and provide sufficient coordination space for large-diameter atoms, which is conducive to modulating the electronic structure of the metal center. Hence, employing HsGDY as a carbon support is promising to create a novel class of anchor sites for catalysts with high-performance.

Here, we propose a facile strategy to construct asymmetric anchor sites by taking advantage of unique structure of HsGDY, where the Mn single atoms are shown to be coordinated with two types of N and OH ligands. Density functional theory (DFT) calculations reveal that the encouraging performance of Mn-N-HsGDY derives from the synergistic coordination of electron-withdrawing sp-N and OH ligands, which empowers easy desorption of *OH, thus improving the ORR activity. As a result, the Mn-N-HsGDY exhibits an excellent ORR performance and superior long-term stability. Specifically, the liquid-state Zn-air batteries (ZABs) assembled with Mn-N-HsGDY delivers an impressive power density of 276.5 mW cm⁻² and extraordinary durability for 3800 cycles with no obvious degradation, surpassing benchmark Pt/C-IrO₂ and a great mass of the state-of-the-art SACs. This finding not only explores an easy way to prepare asymmetric active sites, but also opens up a unique insight in terms of substrate selection and structure modification.

2. Experimental

2.1. Synthesis of Mn-N-HsGDY

HsGDY (20 mg) and a few anhydrous MnCl₂ were dispersed in deionized water by ultrasound and stirred overnight. Subsequently, the mixture was washed with abundant deionized water to remove weakly adsorbed and excess ions. Then, the mixture was dried under vacuum to obtain powder sample. The obtained powder was calcined in a NH₃ atmosphere at 800 °C, 900 °C, and 1000 °C, respectively, for 30 min to get Mn-N-HsGDY catalysts treated different temperature.

2.2. Synthesis of the control samples

N-HsGDY and Mn-HsGDY samples were prepared with similar procedure without adding Mn source or NH₃, respectively.

2.3. Characterizations

The morphologies and microstructures were characterized by SEM (Zeiss Gemini SEM 300 field emission scanning electron microscope), TEM (Hitachi HT7700 Transmission Electron Microscope) at an acceleration voltage of 200 kV, HRTEM (JEOL JEM-2100F), respectively. The images of HAADF-STEM and corresponding STEM mapping were obtained by a FEI-Titan Cubed Themis G2 300 equipped with energy-dispersive X-ray spectroscopy (EDX). The crystal phases were studied by X-ray diffraction (XRD) on a Japan Rigaku SmartLab 9 kW. Raman measurement was performed on a LabRAM HR800 Confocal Raman Spectrometer with 473 nm excitation laser light. XPS spectra were collected on a Kratos AXIS Supra spectrometer with Al K α radiation as the excitation sources. The BET surface area was obtained by ASAP 2460-4MP at 77 K and the pore size distribution was calculated from the corresponding nitrogen absorption and desorption isotherm. The Mn content of the as-synthesized catalyst was determined by inductive coupled plasma mass spectrometry (ICP-MS) (NexION 350X). X-ray absorption fine structure (XAFS) experiments were carried out at the 4B7A station in Beijing Synchrotron Radiation Facility.

2.4. Electrochemical measurements

First, 5 mg catalyst was blended with 50 μ L Nafion (5 wt%) and 950 μ L ethanol and then sonicated until the mixture yielded a fine ink. Next, the catalyst ink was pipetted onto the glassy carbon rotating ring disk electrode (RRDE) and the loadings on RRDE achieved 0.4 mg cm⁻². After naturally drying, an electrode coated with catalyst film was obtained. All the electrochemical measurements were performed on a CHI 760E electrochemical workstation. A three-electrode cell, in which a saturated calomel electrode (SCE) and a Pt foil were used as reference electrode and counter electrode, respectively. A RRDE (4 mm in diameter) was used as working electrode. In test, 0.1 M HClO₄ and 0.1 M KOH solution were employed as acidic and alkaline electrolytes, respectively. All potentials mentioned in the electrochemical measurements were calibrated relative to the reversible hydrogen electrode (RHE). Before the test, the electrolyte in the cell was saturated with N₂ or O₂ for 30 min. The activity of the catalyst was determined by liner sweep voltammetry (LSV) in the potential of 0–1.2 V at a rotating speed of 1600 rpm with a sweep rate of 5 mV s⁻¹ in O₂-saturated electrolytes, while the ring electrode was held at 1.3 V vs RHE. The ORR stability tests were conducted by continuous potential cycling in O₂-saturated electrolytes between 0.6 V and 1.2 V at a scan rate of 100 mV s⁻¹. After 5000 cycles, the LSV curves were measured in O₂-saturated solution with a sweep rate of 5 mV s⁻¹ and a rotation speed at 1600 rpm. The methanol tolerance measurements were performed by comparing the LSV curves before and after methanol addition. The electron transfer number (n) and the %H₂O₂ released during ORR were calculated by RRDE tests. The calculation formula is as follows:

$$n = \frac{4I_D}{I_D + (I_R/N)}$$

$$\%H_2O_2 = 100 \frac{2I_R/N}{I_D + (I_R/N)}$$

where I_D is the absolute value of Faradaic current at the disk, I_R the absolute value of Faradaic current at the ring and N is the H₂O₂ collection coefficient at the ring. Furthermore, the electron transfer number can be also calculated by the LSV curves at different rotation speeds based on the Koutechy-Levich equation:

$$\frac{1}{j} = \frac{1}{j_L} + \frac{1}{j_k} = \frac{1}{B\omega^{1/2}} + \frac{1}{j_k}$$

$$B = 0.62nFC_0(D_0)^{2/3}\nu^{-1/6}$$

where j is measured current density, j_k is kinetic current density, j_L is diffusion limited current density, ω is electrode rotation rate, F is Faraday constant (96,485 C mol⁻¹), C_0 is bulk concentration of O₂ (1.2×10^{-3} mol L⁻¹), D_0 is diffusion coefficient of O₂ (1.9×10^{-5} cm² s⁻¹) and ν is kinetic viscosity of the electrolyte (0.01 cm² s⁻¹).

3. Results and discussions

As shown in Fig. 1a, graphene-like substrates feature with dense benzene ring structures and high atomic density, which create symmetric M-N₄ sites generally. Thus, it is challenging to introduce large-sized heteroatoms, such as OH, into the framework. HsGDY, with abundant inherent edge-rich carbon domain, generates asymmetric M-N₂ sites and offers a conducive environment for the introduction of large heteroatoms. The scanning electron microscopy (SEM) and transmission electron microscopy (TEM) images show that the as-synthesized catalysts retain a porous structure consistent with the morphology of HsGDY (Fig. 1b, c and Fig. S2–S10). In addition, no Mn nanoparticles are observed in the TEM images of Mn-N-HsGDY, which is also approved by the X-ray diffraction (XRD) measurement without diffraction peaks of Mn species (Fig. 1c and Fig. S11). Further, the abundant bright dots

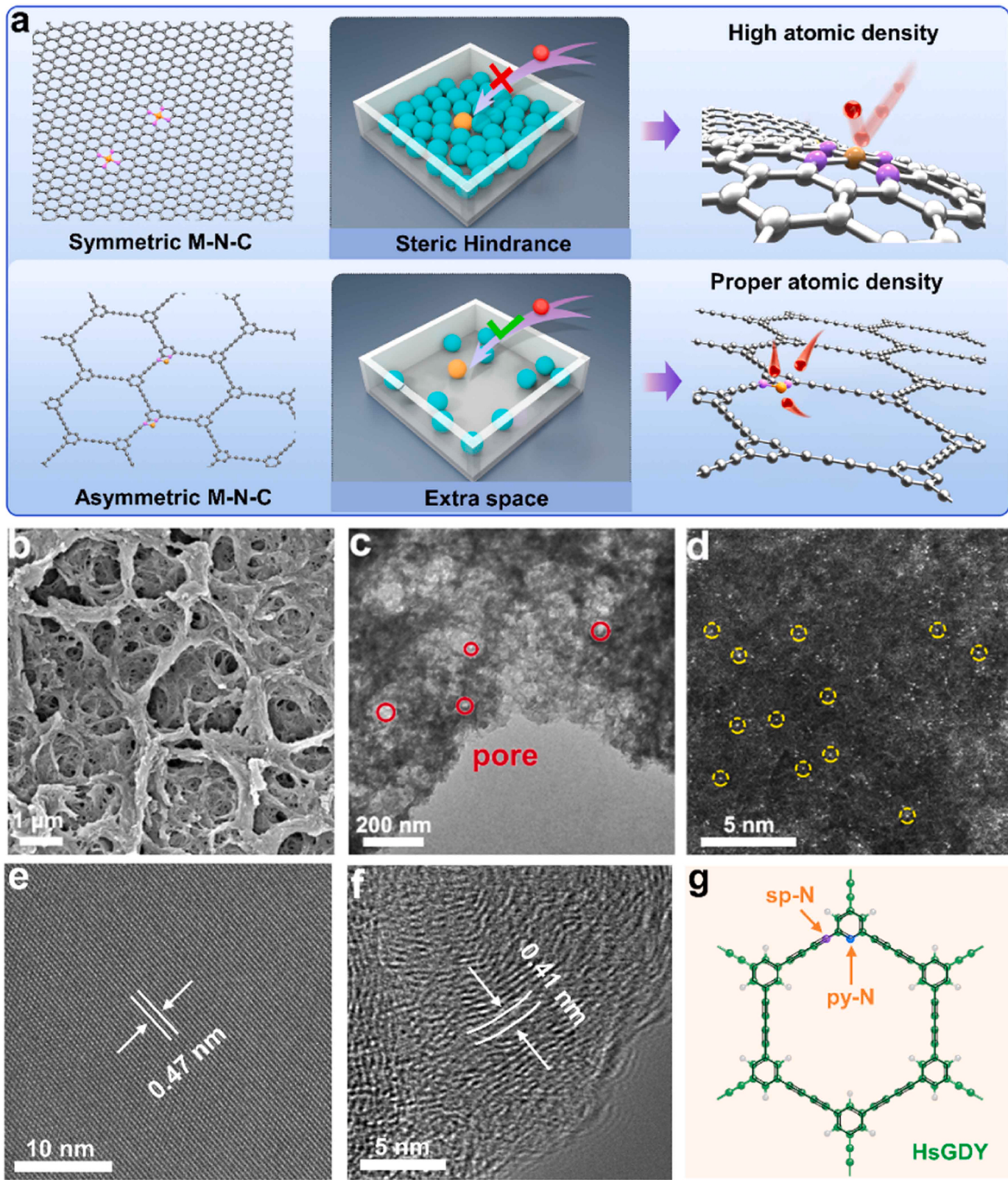


Fig. 1. Schematic illustration and morphology characterization of Mn-N-HsG DY. (a) Schematic illustration of introducing OH into graphene and HsG DY. (b) SEM image, (c) Low resolution TEM image, (d) AC HAADF-STEM image and (e,f) High-resolution TEM images of Mn-N-HsG DY. (g) Nitrogen doping positions in HsG DY.

observed by aberration-corrected high-angle annular darkfield scanning transmission electron microscopy (AC HAADF-STEM) correspond to single Mn atoms (Fig. 1d and Fig. S12), indicating that Mn species are atomically dispersed. The high-resolution transmission electron

microscopy (HRTEM) images show that the lattice fringes and interlayer stripper of Mn-N-HsG DY agree well with HsG DY (Figs. 1e and 1f) [37–39].

To investigate the surface composition and chemical structure of

catalysts, X-ray photoelectron spectroscopy (XPS) measurements were carried out. The C 1s spectra can be mainly fitted into four subpeaks, corresponding to C-C (sp^2), C-C (sp), C-O and C=O, respectively (Fig. S13). The area ratio of sp^2 -C/sp-C is close to 1:1, consistent with HsGDY [27,29]. Besides, HsGDY and Mn-N-HsGDY exhibit nearly identical C K-edge curves and Raman spectra (Fig. S14 and S15). All these results indicate that the carbon skeleton structure of HsGDY is preserved in the Mn-N-HsGDY. The N 1s XPS spectrum of Mn-N-HsGDY displays two characteristic peaks at 397.6 eV and 399.9 eV (Fig. S16), corresponding to sp-N and pyridinic N as shown in Fig. 1g. The N chemical states are also probed by the N K-edge XANES. The two peaks of N K-edge spectrum (Fig. S17) derive from sp-N (398.3 eV) and

pyridinic N (401.3 eV), which is in accord with the XPS results. As determined by inductively coupled plasma-mass spectrometry (ICP-MS), the atomic content of Mn in Mn-N-HsGDY is 1.8 wt%. The surface area of Mn-N-HsGDY calculated from the N_2 adsorption/desorption isotherm is as high as $959\text{ m}^2\text{ g}^{-1}$, which is conducive to the creation and exposure of the active site (Fig. S18a). The pore size is mainly distributed in the micropore, but there is a small hysteresis loop at higher pressure region (Fig. S18b), indicating the existence of mesopores and macropores, which facilitates the mass transfer during the electrochemical process.

Notably, when only N is introduced, only pyridinic N is formed for N-HsGDY (Fig. S19), which coincides well with previous reports [32]. However, when Mn atoms are introduced (Fig. S20), sp-N is also formed

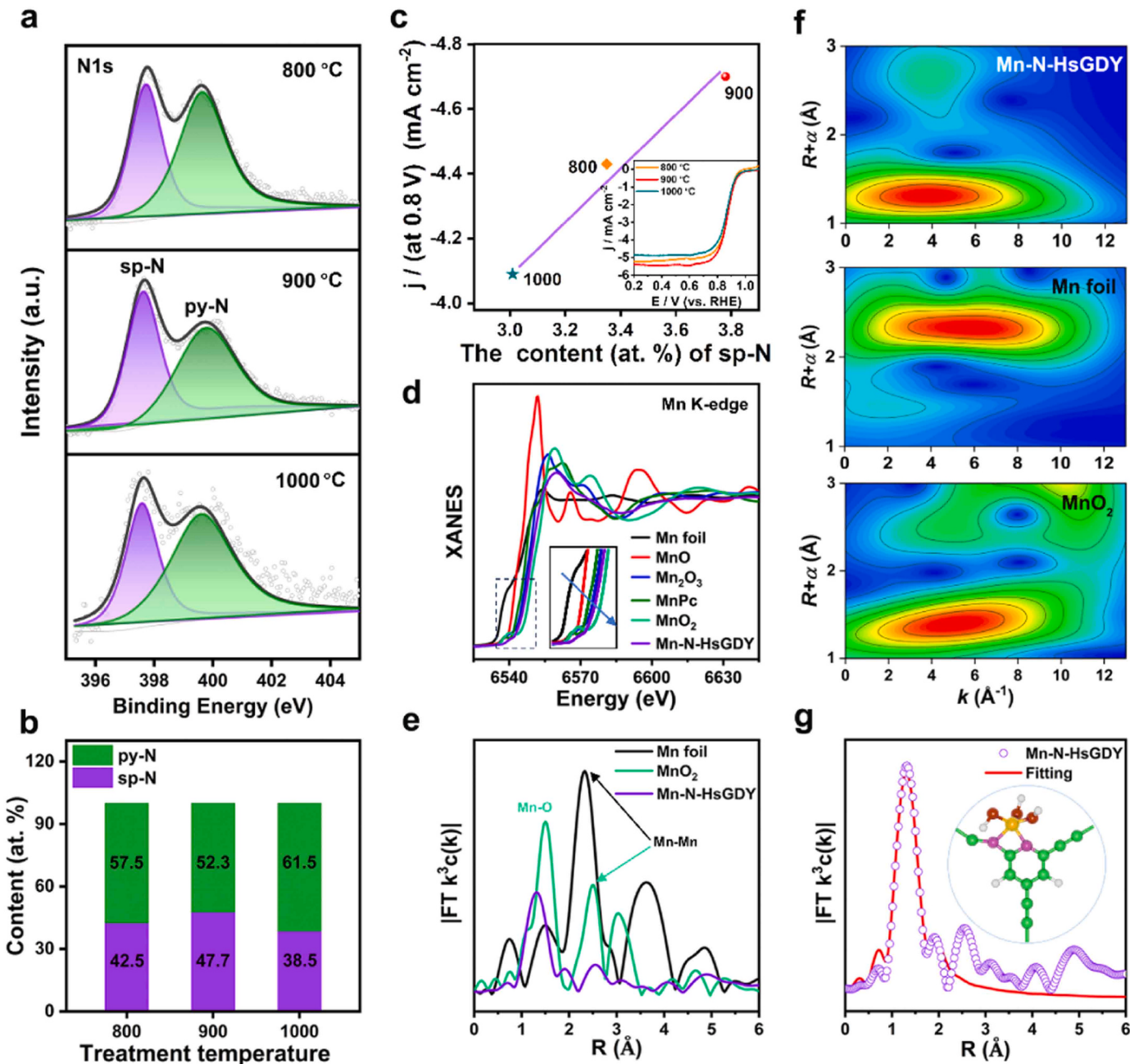


Fig. 2. Atomic structural analysis of Mn-N-HsGDY. (a) N 1s XPS spectra and (b) the corresponding N species contents in Mn-N-HsGDY synthesized at different temperatures. (c) Linear relationship between the absolute content of sp-N and ORR activity of the catalysts. Inset: The LSV curves of Mn-N-HsGDY annealed at different temperatures. (d) Mn K-edge XANES spectra of Mn-N-HsGDY and reference samples. (e) Fourier-transformed (FT) of the Mn K-edge EXAFS spectra of Mn-N-HsGDY along with the reference samples. (f) Wavelet Transforms of Mn-N-HsGDY, Mn foil, and MnO_2 , respectively. (g) FT-EXAFS fitting curves of Mn-N-HsGDY at R space. Insert: Atomic structure model for Mn-N-HsGDY (Mn, yellow; C, green; N, purple; O, red).

in addition to pyridine N. To disclose the role of sp-N in the formation of active sites, we synthesized Mn-N-HsGDY treated in different temperatures (800 °C, 900 °C, and 1000 °C) and investigated the N 1s XPS spectra of these catalysts. In detail, all the three catalysts display two peaks that correspond to sp-N and pyridinic N, respectively (Fig. 2a). From the XPS survey spectra of Mn-N-HsGDY (Fig. S21), it can be seen that the total content of nitrogen in the catalysts prepared at different temperatures is close. Then, we calculate the ratios of sp-N and pyridine nitrogen based on the N 1s spectra and find that it reaches the maximum of 47.7 % at 900 °C, higher than the other two catalysts (Fig. 2b). Meanwhile, the ORR activities of these three catalysts were tested (inset in Fig. 2c) and it was found that there is a strong correlation between the absolute content of sp-N and the activity of the catalysts (Fig. 2c). As the sp-N content increases, the ORR performances of the catalysts are improved gradually. The catalyst heat-treated at 900 °C achieves the best activity due to the creation of more active sites at this temperature. This result corroborates that sp-N is coordinated with Mn atom and involved in the fabrication of active sites. In addition, Mn atoms may be coordinated with oxygen-containing functional groups, as evidenced by a Mn-O peak in the O 1s XPS spectrum of Mn-N-HsGDY (Fig. S22).

To further identify the local structure of the Mn atoms in the Mn-N-HsGDY, X-ray absorption spectroscopy (XAS) was performed. A comparison of the energies of the Mn K-edges in X-ray absorption near-edge structure (XANES) spectra for Mn-N-HsGDY with the control samples, indicates that the isolated Mn atoms bear a positive charge between +3 and +4 (Fig. 2d and Fig. S23). The high valence state of Mn atom stems from the charge transfer from Mn to its adjacent N and O atoms. The high oxidation state of Mn sites is favorable for the desorption of *OH in the ORR process and thus enhances its catalytic performance [36,40]. The Fourier transform (FT) extended X-ray absorption fine structure (EXAFS) spectrum of Mn-N-HsGDY is dominated by a scattering path at approximately 1.3 Å, assigned to the Mn-N/O configuration [5]. Absence of Mn-Mn scattering path at ~2.3 Å (existing in both Mn foil and MnO₂), reveals the atomic dispersion of Mn in Mn-N-HsGDY (Fig. 2e). Meanwhile, wavelet transform (WT) analysis was resorted to discriminate the atomic configuration due to the high resolutions in both *k* and R spaces. The WT spectrum of Mn-N-HsGDY detected an intensity maximum at ~4 Å⁻¹, which could be assigned to the Mn-N/O contributions, while the signal corresponding to Mn-Mn scattering was absent (Fig. 2f). Further, the coordination configuration of Mn was analyzed by

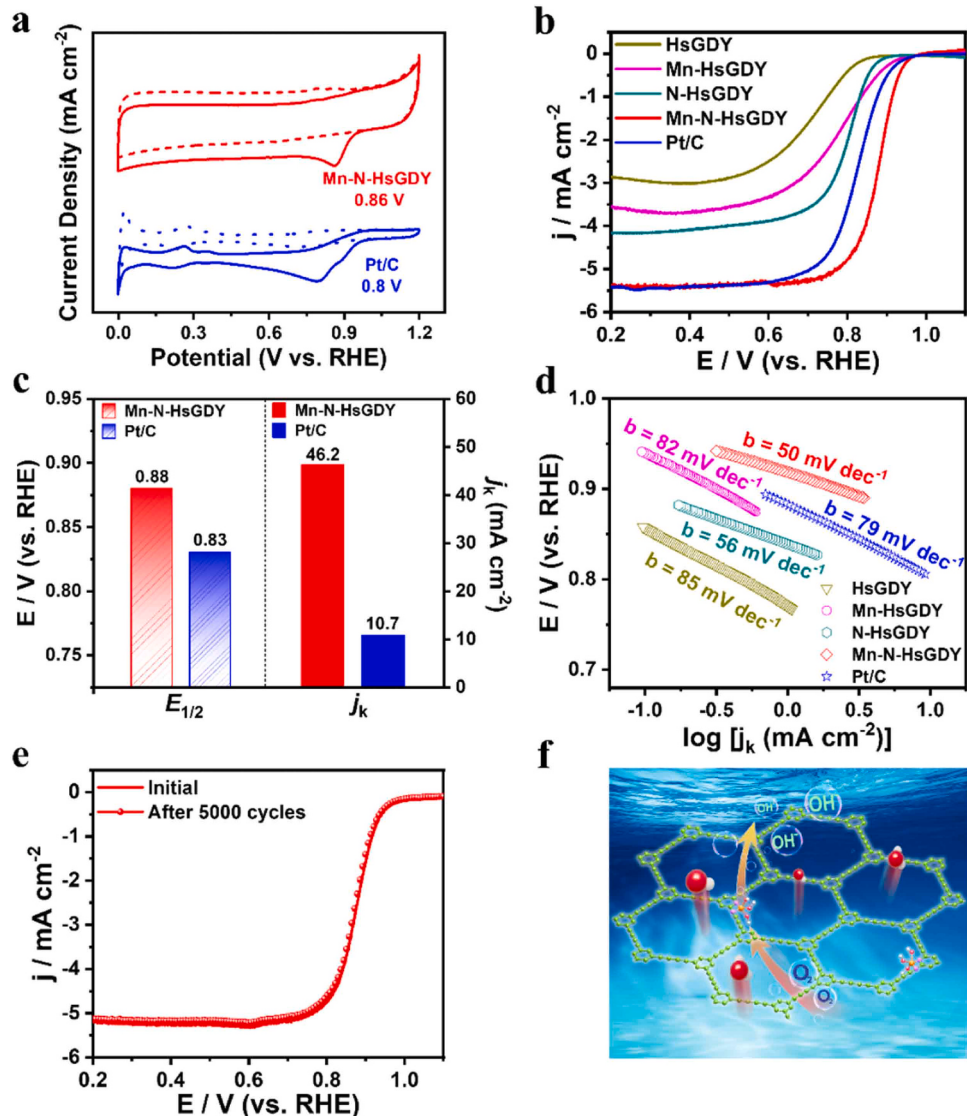


Fig. 3. Electrochemical performances of Mn-N-HsGDY for ORR. (a) CV curves of Pt/C and Mn-N-HsGDY measured in Ar (dashed line) and O₂ (solid line) saturated 0.1 M KOH solution. (b) ORR polarization curves of Mn-N-HsGDY, Pt/C and control samples in O₂-saturated 0.1 M KOH solution. (c) Values of J_k at 0.80 V and $E_{1/2}$ for Pt/C and Mn-N-HsGDY. (d) Tafel plots for all catalysts. (e) ORR polarization curves of Mn-N-HsGDY before and after 5000 CV cycles. (f) Schematic diagram of ORR on Mn-N-HsGDY.

quantitative least-square EXAFS fitting (Fig. 2g) and the structural parameters were summarized in Table S1. The best-fitting result of Mn-N-HsGDY demonstrates that the coordination number for N and O atoms are calculated as 2 and 3, respectively. Combined with the results of XPS and theoretical calculations, the atomic structure model of Mn site is determined as $\text{MnN}_2(\text{OH})_3$ (inset in Fig. 2g).

The ORR tests were evaluated in 0.1 M KOH electrolyte using a rotating ring-disk electrode (RRDE). Firstly, the cyclic voltammetry (CV) curves of Mn-N-HsGDY and Pt/C were measured in Ar and O_2 saturated conditions. Mn-N-HsGDY displays a more positive cathodic peak than that of Pt/C, indicating its higher catalytic activity (Fig. 3a). Linear sweep voltammetry (LSV) curves reveal that Mn-N-HsGDY exhibits the

best ORR activity among all samples with a more positive half-wave potential ($E_{1/2}$) of 0.88 V and a higher onset potential of 1.01 V (Fig. 3b). The Mn-N-HsGDY reaches a kinetic current density (J_k) of 46.2 mA cm^{-2} at 0.80 V, about 4 times that of Pt/C (10.7 mA cm^{-2}) (Fig. 3c). Furthermore, the J_k of Mn-N-HsGDY is significantly greater than that of Pt/C at various potential, evidencing its faster ORR kinetics (Fig. S24), which is also verified by a lower Tafel slope of 50 mV dec^{-1} than the Pt/C counterpart (79 mV dec^{-1}) (Fig. 3d). The optimal loading of Mn-N-HsGDY was investigated by testing the activities of the catalyst with a series of loadings. The optimal loading of Mn-N-HsGDY is tested as 0.4 mg cm^{-2} (Fig. S26). The catalytic selectivity of Mn-N-HsGDY towards ORR was evaluated by recording LSV curves at different rotation

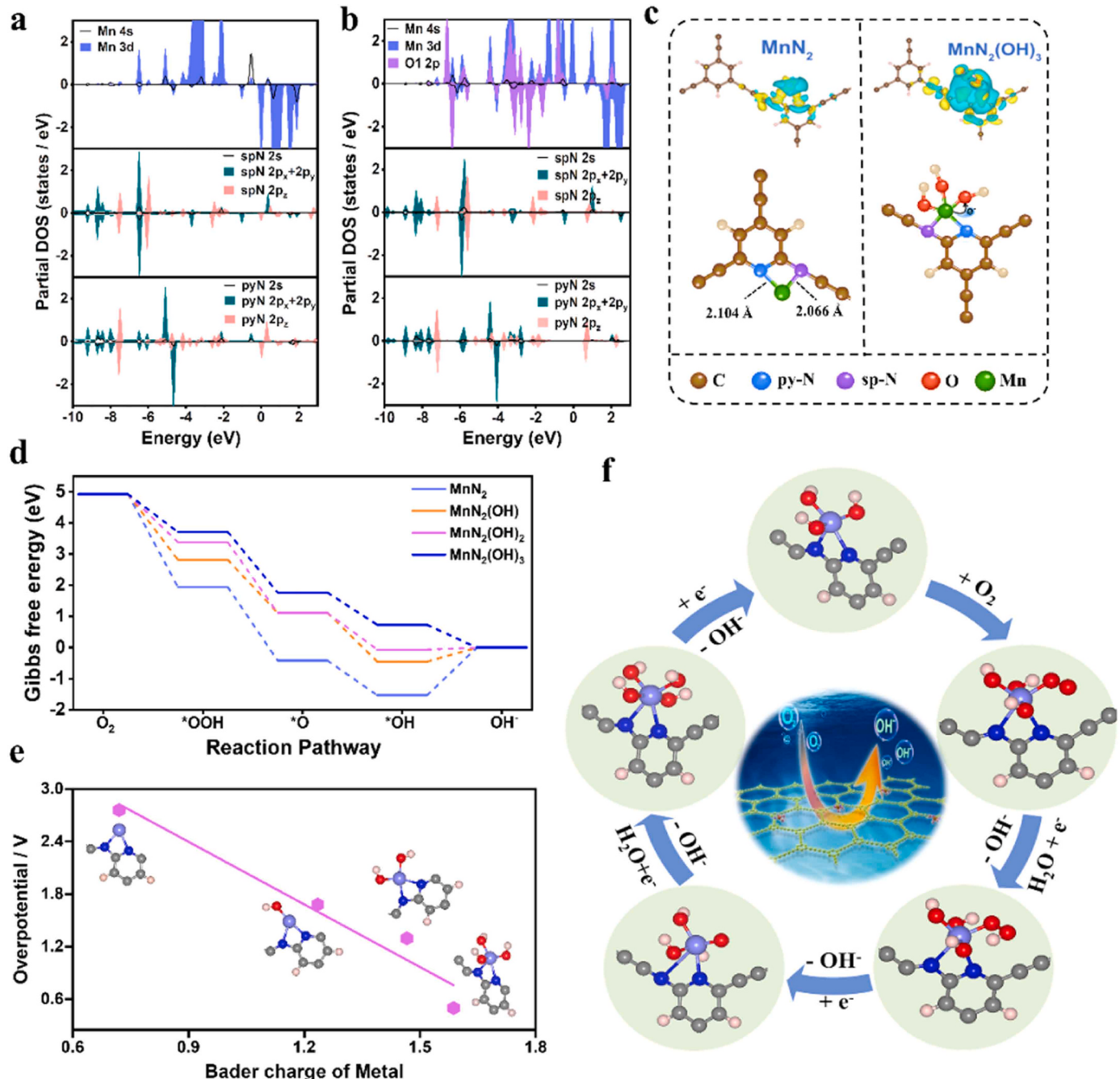


Fig. 4. Theoretical ORR activity of Mn-N-HsGDY. (a) The calculated DOS of Mn site, sp-N, and py-N for MnN_2 configuration. (b) The DOS of Mn site, sp-N, py-N and O 2p for $\text{MnN}_2(\text{OH})_3$ configuration. (c) Charge density difference and bonding information for MnN_2 and $\text{MnN}_2(\text{OH})_3$. (d) Linear relationship between the ORR overpotential and the Bader charge of Mn center in $\text{MnN}_2(\text{OH})_x$ ($x = 0, 1, 2, 3$) configurations. (e) Gibbs free energy diagrams for ORR on $\text{MnN}_2(\text{OH})_x$ ($x = 0, 1, 2, 3$) at $U = 0 \text{ V}$ vs. RHE. (f) The proposed ORR mechanism on $\text{MnN}_2(\text{OH})_3$. C: grey; N: blue; O: red; Mn: pink.

speeds. By fitting the Koutecky-Levich (K-L) plots, the electron transfer number is calculated to be 3.92–3.98, indicating a high-efficiency $4e^-$ pathway (Fig. S27). Besides, the RRDE measurement was also conducted. The calculated electron-transfer number is consistent with the result of K-L plots and the yield of H_2O_2 is as low as 7 % during the reaction process, which further confirms that a direct $4e^-$ pathway is preferable (Fig. S28). In addition, methanol resistance test indicates that methanol has little effect on the activity of Mn-N-HsGDY, whereas there is an evident methanol oxidation peak for Pt/C (Fig. S29). The stability of Mn-N-HsGDY was evaluated by comparing the LSV curves before and after a 5000 cycles CV test. Obviously, Mn-N-HsGDY displays a negligible shift in $E_{1/2}$, while Pt/C shows a significant $E_{1/2}$ shift of 35 mV (Fig. 3e and Fig. S30a). The exceptional activity and superior stability of Mn-N-HsGDY benefit from the strong coupling effect between active Mn atoms and the substrate. The intrinsic asymmetry of HsGDY directly results in the formation of asymmetric sites, which further regulates the electronic structure of center metal and makes the Mn atoms firmly bound to the substrate. Fig. 3f shows the schematic diagram of the ORR process on the Mn-N-HsGDY. Meanwhile, the ORR activity of Mn-N-HsGDY is studied as well in 0.1 M $HClO_4$ (Fig. S34–S38).

Density functional theory (DFT) calculations were conducted to gain a further insight into the underlying mechanism at the atomic level of the excellent ORR performance of Mn-N-HsGDY. The calculation details are provided in [Supporting information](#). Firstly, the density of states (DOS) is investigated. Obviously, the bonding states formed by the hybridization of sp-N 2p states and Mn 3d states appear around -6.2 eV below the Fermi level, which is deeper than that of forming by py-N 2p states with Mn 3d states (Fig. 4a). Correspondingly, the bond length of Mn-N (sp) is slightly shorter than that of Mn-N (py) (Fig. 4c), which indicates a stronger chemical bonding strength of sp-N and Mn. These results demonstrate that sp-N has a greater impact on the 3d state of Mn than py-N. Besides, the elegant molecular pores of HsGDY endow metal atoms with available space to be coordinated with terminal ligands (OH), which further modulates the electronic structure of central metal. As shown in Fig. 4b, the O 2p states are strongly hybridized with the Mn 3d states. The Mn 3d band center can be downshifted by coordinated with the electron-withdrawing OH groups [41,42] which is attributed to the charge transfer occurring at the Mn-OH interface besides the well-known Mn-N interface (Fig. 4c). Based on the structure resolved by XANES and EXAFS, four types of single Mn atom models are constructed, i.e., $MnN_2(OH)_x$ ($x = 0, 1, 2$, and 3) (Fig. S39 and S40). As shown in Fig. 4d, the rate-determining step (RDS) of ORR for all proposed models is the *OH desorption ($^*OH + e^- \rightarrow ^* + OH$). Besides, all the elementary reactions on the site of $MnN_2(OH)_3$ is exothermic, that is, thermodynamically favorable, while the other three models are endothermic in the RDS, at 0 V vs RHE (Fig. S41). Meanwhile, the ORR processes at $U = 1.23$ V are also conducted (Fig. S42). The energy barrier of the RDS on $MnN_2(OH)_3$ is the lowest (0.502 eV) compared to the other three models, demonstrating its rapid kinetics for the ORR. Further insights into the effect of different number of OH ligands on the performance of the active sites were investigated. As the number of OH ligands increase, the Bader charge of the metal center also increases gradually (Fig. S43), which results in a weak binding to *OH (Fig. S44). This is also verified by the linear plots of the ORR overpotential and the Bader charge (which is correlated to the nominal oxidation state) of metal center (Fig. 4e). As the Bader charge of Mn increases, it is favorable for the desorption of *OH , which in turns boosts the ORR performance. Thus, the superiority of $MnN_2(OH)_3$ for ORR is originated from the asymmetric coordination of sp-N and OH ligands, which weakens the adsorption of *OH on the Mn center to promote the ORR process. The proposed mechanism of ORR on the $MnN_2(OH)_3$ is presented in Fig. 4f.

Inspired by the excellent ORR performance, a liquid-state ZAB assembled with Mn-N-HsGDY as an air cathode and a fresh zinc sheet as the anode was fabricated to explore its practical application (Fig. 5a). The open-circuit voltage (OCV) of the ZAB assembled with Mn-N-HsGDY is 1.56 V, which is higher than that of Pt/C-IrO₂ (1.50 V). Two ZABs in

series can power a car-shaped light (Fig. S45). The entire LSV curves of Mn-N-HsGDY and Pt/C-IrO₂ for ORR and oxygen evolution reaction (OER) were measured to evaluate the bifunctional activities by corresponding potential gap (ΔE). The Mn-N-HsGDY exhibits a low ΔE of 0.71 V (Fig. 5b), which is smaller than that of Pt/C-IrO₂ (0.76 V) and exceeds most recently reported carbon-based catalysts (Table S3). The Mn-N-HsGDY-based battery generates a larger specific capacity of 810 mA h g⁻¹ than that of Pt/C-IrO₂-based ZAB (641 mA h g⁻¹), which indicates a good energy storage capacity (Fig. S46). Remarkably, the maximum power density of Mn-N-HsGDY calculated by the discharge curve is 276.5 mW cm⁻², which is 2.7 times that of Pt/C-IrO₂ (101 mW cm⁻²) and surpasses most of the state-of-the-art non-precious metal catalysts to the best of our knowledge (Fig. 5c, e and Table S3). Additionally, the discharge curves of Mn-N-HsGDY-based battery at different current densities were measured and the potential retention was 99.9 % (Fig. 5d), indicating a superior rate performance. Subsequently, the long-term stability was evaluated by galvanostatic discharging/charging test at 2 and 5 mA cm⁻², respectively. Excitingly, the Mn-N-HsGDY-based battery steadily operates up to 3800 cycles at 2 mA cm⁻², where the round-trip voltage changes from 0.83 V at the beginning to 0.86 V (Fig. 5f). In contrast, the battery with Pt/C-IrO₂ as air cathode fails fleetly with limited cycling capacity (Fig. S48). Moreover, even at a high current of 5 mA cm⁻², the Mn-N-HsGDY-based battery can also run stably for 950 cycles with a voltage gap of 0.87 V and no obvious voltage degradation is observed throughout the process (Fig. 5g). The extraordinary durability of the Mn-N-HsGDY-based battery outperforms most of the reported advanced ZABs (Fig. 5e) [43–46]. In addition, the morphology and structure of Mn-N-HsGDY after a long cycle test were characterized. The pore structure can be observed from SEM and TEM images (Fig. S49–50) and the XPS spectra show that the chemical composition and structure of the catalyst is almost maintained. Together, the high-power density, desirable rate performance and extraordinary long-term stability unveil that Mn-N-HsGDY is a potential catalyst for rechargeable ZABs.

In addition, one-dimensional (1D) and two-dimensional (2D) solid-state ZABs were fabricated to study the feasibility of its practical application in flexible and wearable technologies (See [Section 2](#) for details). As displayed in Fig. 5h, the assembled 1D ZAB generates a stable OCV of 1.363 V and maintains a relatively stable potential gap at 1 mA cm⁻² under different bending states of straight, one ring, and two rings. Furthermore, a 1D ZAB in the bent state can keep a timer working well, showing its good flexibility and potential for practical application. Meanwhile, 2D ZAB based on Mn-N-HsGDY also exhibits a small voltage gap in the charging/discharging cycling test during the 1400 min, as well as a constant OCV of 1.249 V under different bending. Impressively, the assembled 2D ZAB delivers a high peak power density of 156.6 mW cm⁻², which is superior to that of most recently reported flexible ZABs [47,48]. Three 2D ZABs in series can illuminate a “SDU”-shaped LED light with a minimum operating voltage of 3 V (Fig. S51). The excellent performances of Mn-N-HsGDY in solid-state ZABs indicate that it is competitive for the application of wearable energy devices.

4. Conclusions

In summary, we have developed a novel strategy that can directly construct asymmetric catalytic sites by the rational design of carbon substrate. The Mn SAC prepared by this method exhibits excellent ORR activity. The XAS analyses demonstrate that Mn is coordinated with two types of N and OH ligands simultaneously to form an asymmetric active site. DFT calculations further reveal that the active sites mainly enhance ORR activity by facilitating *OH desorption, which coincides well with the experimental results. Benefiting from the competitive ORR performance, the Mn-N-HsGDY-based liquid-state ZAB delivers a high-power density and demonstrates remarkable long-term durability, exceeding Pt-based catalysts as well as most state-of-the-art non-precious metal

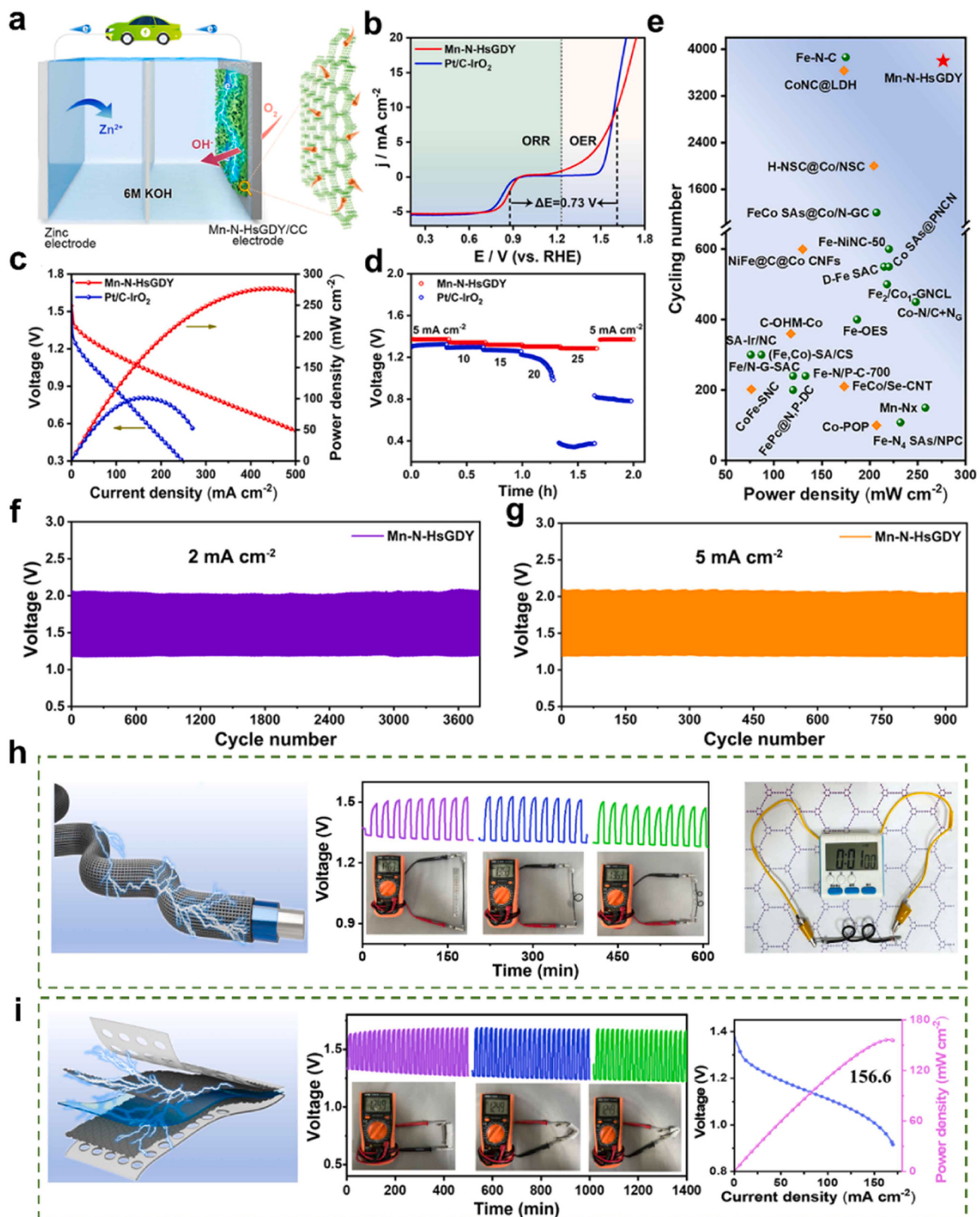


Fig. 5. Performance of Mn-N-HsGDY in ZABs. (a) The schematic illustration of ZAB assembled with Mn-N-HsGDY. (b) Overall polarization curves for Mn-N-HsGDY and Pt/C-IrO₂ between the ORR and OER potential window. (c) Discharge curves and corresponding power density and (d) rate performance of rechargeable ZABs using the Mn-N-HsGDY and Pt/C-IrO₂ cathodes. (e) Comparison of Mn-N-HsGDY (red star) with recently reported SAC-based catalysts (green ball) and other non-noble metal catalysts (orange square) in terms of peak power density and long-term cycle stability in ZABs. (f,g) Cycling stability of ZABs assembled with Mn-N-HsGDY air electrode at current density of 2 mA cm⁻² and 5 mA cm⁻², respectively. (h,i) The performance of homemade solid 1D/2D ZABs assembled with Mn-N-HsGDY.

catalysts. Moreover, Mn-N-HsGDY, as an air cathode for the flexible solid-state ZAB, exhibits good cyclic stability at various bending states, indicating its application potential in flexible electronic devices. This work provides a new perspective for the preparation of highly active asymmetric catalytic sites by designing specific carbon supports. Besides, through mechanism analysis at the atomic level, our findings are of great significance for further understanding the structure-activity relationship of catalysts and expand research ideas for the exploitation of other energy-conversion-related catalysts.

CRediT authorship contribution statement

Xingru Yan: Data curation. **Xiangyao Gu:** Investigation. **Xiaodong Li:** Visualization, Data curation. **Zhufeng Hou:** Software, Methodology, Formal analysis, Data curation. **Meiping Li:** Writing – original draft, Visualization, Investigation, Formal analysis, Data curation, Conceptualization. **Changshui Huang:** Writing – review & editing, Writing – original draft, Visualization, Supervision, Project administration, Methodology, Conceptualization. **Qing Lv:** Writing – review & editing, Validation, Supervision, Project administration.

Declaration of Competing Interest

The authors declare that they have no known competing financial interests or personal relationships that could have appeared to influence the work reported in this paper.

Data availability

Data will be made available on request.

Acknowledgements

This work was supported by the National Natural Science Foundation of China (No. 22172090), the National Key Research and Development Project of China (2022YFA1204500, 2022YFA1204501), the strategic priority research program of the Chinese Academy of Sciences (XDB0520200), the Natural Science Foundation of Shandong Province (ZR2021MB015), the Open Funds of the State Key Laboratory of Electroanalytical Chemistry (SKLEAC202202), the Young Scholars Program of Shandong University, Beijing National Laboratory for Molecular Sciences and Postdoctoral Fellowship Program of CPSF.

Appendix A. Supporting information

Supplementary data associated with this article can be found in the online version at [doi:10.1016/j.apcatb.2024.124249](https://doi.org/10.1016/j.apcatb.2024.124249).

References

- [1] Y. Liu, X. Liu, Z. Lv, R. Liu, L. Li, J. Wang, W. Yang, X. Jiang, X. Feng, B. Wang, Tuning the spin state of the iron center by bridge-bonded Fe-O-Ti ligands for enhanced oxygen reduction, *Angew. Chem. Int. Ed.* 61 (2022) e202117617, <https://doi.org/10.1002/anie.202117617>.
- [2] H. Fei, J. Dong, Y. Feng, C.S. Allen, C. Wan, B. Voloskiy, M. Li, Z. Zhao, Y. Wang, H. Sun, P. An, W. Chen, Z. Guo, C. Lee, D. Chen, I. Shakir, M. Liu, T. Hu, Y. Li, A. I. Kirkland, X. Duan, Y. Huang, General synthesis and definitive structural identification of MN_4C_4 single-atom catalysts with tunable electrocatalytic activities, *Nat. Catal.* 1 (2018) 63–72, <https://doi.org/10.1038/s41929-017-0008-y>.
- [3] Q. Wang, Q. Feng, Y. Lei, S. Tang, L. Xu, Y. Xiong, G. Fang, Y. Wang, P. Yang, J. Liu, W. Liu, X. Xiong, Quasi-solid-state Zn-air batteries with an atomically dispersed cobalt electrocatalyst and organohydrogel electrolyte, *Nat. Commun.* 13 (2022) 3689, <https://doi.org/10.1038/s41467-022-31383-4>.
- [4] C. Zhou, X. Chen, S. Liu, Y. Han, H. Meng, Q. Jiang, S. Zhao, F. Wei, J. Sun, T. Tan, R. Zhang, Superdurable bifunctional oxygen electrocatalyst for high-performance zinc-air batteries, *J. Am. Chem. Soc.* 144 (2022) 2694–2704, <https://doi.org/10.1021/jacs.1c11675>.
- [5] J. Li, M. Chen, D.A. Cullen, S. Hwang, M. Wang, B. Li, K. Liu, S. Karakalos, M. Lucero, H. Zhang, C. Lei, H. Xu, G.E. Sterbinsky, Z. Feng, D. Su, K.L. More, G. Wang, Z. Wang, G. Wu, Atomically dispersed manganese catalysts for oxygen reduction in proton-exchange membrane fuel cells, *Nat. Catal.* 1 (2018) 935–945, <https://doi.org/10.1038/s41929-018-0164-8>.
- [6] L. Han, H. Cheng, W. Liu, H. Li, P. Ou, R. Lin, H.-T. Wang, C.-W. Pao, A.R. Head, C.-H. Wang, X. Tong, C.-J. Sun, W.-F. Pong, J. Luo, J.-C. Zheng, H.L. Xin, A single-atom library for guided monometallic and concentration-complex multimetallic designs, *Nat. Mater.* 21 (2022) 681–688, <https://doi.org/10.1038/s41563-022-01252-y>.
- [7] Y. Guo, C. Wang, Y. Xiao, X. Tan, W. He, J. Chen, Y. Li, H. Cui, C. Wang, Stabilizing Fe single atom catalysts by implanting Cr atomic clusters to boost oxygen reduction reaction, *Appl. Catal. B* 344 (2024) 123679, <https://doi.org/10.1016/j.apcatb.2023.123679>.
- [8] T. Yang, X. Yang, N. Gao, M. Tang, X. Wang, C. Liu, W. Xing, J. Ge, High density iridium synergistic sites boosting CO-tolerate performance for PEMFC anode, *eScience* (2024) 100230, <https://doi.org/10.1016/j.esci.2024.100230>.
- [9] S. Liu, C. Li, M.J. Zachman, Y. Zeng, H. Yu, B. Li, M. Wang, J. Braaten, J. Liu, H. M. Meyer, M. Lucero, A.J. Kropf, E.E. Alp, Q. Gong, Q. Shi, Z. Feng, H. Xu, G. Wang, D.J. Myers, J. Xie, D.A. Cullen, S. Litster, G. Wu, Atomically dispersed iron sites with a nitrogen-carbon coating as highly active and durable oxygen reduction catalysts for fuel cells, *Nat. Energy* 7 (2022) 652–663, <https://doi.org/10.1038/s41560-022-01062-1>.
- [10] M. Zhao, H. Liu, H. Zhang, W. Chen, H. Sun, Z. Wang, B. Zhang, L. Song, Y. Yang, C. Ma, Y. Han, W. Huang, A pH-universal ORR catalyst with single-atom iron sites derived from a double-layer MOF for superior flexible quasi-solid-state rechargeable Zn-air batteries, *Energy Environ. Sci.* 14 (2021) 6455–6463, <https://doi.org/10.1039/DIEE01602D>.
- [11] G. Luo, E. Zhu, C. Shi, Y. Ren, Y. Lin, X. Yang, M. Xu, Regulating the double-site Mn_2N_6 electronic structure by manganese clusters for enhanced oxygen reduction, *Appl. Catal. B* 350 (2024) 123939, <https://doi.org/10.1016/j.apcatb.2024.123939>.
- [12] L. Zhao, Y. Zhang, L.-B. Huang, X.-Z. Liu, Q.-H. Zhang, C. He, Z.-Y. Wu, L.-J. Zhang, J. Wu, W. Yang, L. Gu, J.-S. Hu, L.-J. Wan, Cascade anchoring strategy for general mass production of high-loading single-atomic metal-nitrogen catalysts, *Nat. Commun.* 10 (2019) 1278, <https://doi.org/10.1038/s41467-019-09290-y>.
- [13] M.D. Hossain, Z. Liu, M. Zhuang, X. Yan, G.-L. Xu, C.A. Gadre, A. Tyagi, I.H. Abidi, C.-J. Sun, H. Wong, A. Guda, Y. Hao, X. Pan, K. Amine, Z. Luo, Rational design of graphene-supported single atom catalysts for hydrogen evolution reaction, *Adv. Energy Mater.* 9 (2019) 1803689, <https://doi.org/10.1002/aenm.201803689>.
- [14] M. Li, H. Wang, W. Luo, P.C. Sherrell, J. Chen, J. Yang, Heterogeneous single-atom catalysts for electrochemical CO_2 reduction reaction, *Adv. Mater.* 32 (2020) 2001848, <https://doi.org/10.1002/adma.202001848>.
- [15] X. Shi, L.N.Y. Cao, M. Chen, Y. Huang, Recent progress on two-dimensional materials confining single atoms for CO_2 photoreduction, *Chin. Chem. Lett.* 33 (2022) 5023–5029, <https://doi.org/10.1016/j.cclet.2022.01.066>.
- [16] L. Gong, H. Zhang, Y. Wang, E. Luo, K. Li, L. Gao, Y. Wang, Z. Wu, Z. Jin, J. Ge, Z. Jiang, C. Liu, W. Xing, Bridge bonded oxygen ligands between approximated FeN_4 sites confer catalysts with high ORR performance, *Angew. Chem. Int. Ed.* 59 (2020) 13923–13928, <https://doi.org/10.1002/anie.202004534>.
- [17] K. Chen, K. Liu, P. An, H. Li, Y. Lin, J. Hu, C. Jia, J. Fu, H. Li, H. Liu, Z. Lin, W. Li, J. Li, Y.-R. Lu, T.-S. Chan, N. Zhang, M. Liu, Iron phthalocyanine with coordination induced electronic localization to boost oxygen reduction reaction, *Nat. Commun.* 11 (2020) 4173, <https://doi.org/10.1038/s41467-020-18062-y>.
- [18] P. Song, B. Hu, D. Zhao, J. Fu, X. Su, W. Feng, K. Yu, S. Liu, J. Zhang, C. Chen, Modulating the asymmetric atomic interface of copper single atoms for efficient CO_2 electroreduction, *ACS Nano* 17 (2023) 4619–4628, <https://doi.org/10.1021/acsm.nano.2c10701>.
- [19] L. Wang, B. Ji, Y. Zheng, Y. Tang, Asymmetric coordination of iridium single-atom IrN_3 boosting formic acid oxidation catalysis, *Angew. Chem. Int. Ed.* 62 (2023) e202301711, <https://doi.org/10.1002/anie.202301711>.
- [20] M. Xiao, Y. Chen, J. Zhu, H. Zhang, X. Zhao, L. Gao, X. Wang, J. Zhao, J. Ge, Z. Jiang, S. Chen, C. Liu, W. Xing, Climbing the apex of the ORR volcano plot via binuclear site construction: electronic and geometric engineering, *J. Am. Chem. Soc.* 141 (2019) 17763–17770, <https://doi.org/10.1021/jacs.9b08362>.
- [21] H. Sun, S. Liu, M. Wang, T. Qian, J. Xiong, C. Yan, Updating the intrinsic activity of a single-atom site with a P=O bond for a rechargeable Zn-air battery, *ACS Appl. Mater. Interfaces* 11 (2019) 33054–33061, <https://doi.org/10.1021/acsmami.9b11337>.
- [22] X.-P. Yin, H.-J. Wang, S.-F. Tang, X.-L. Lu, M. Shu, R. Si, T.-B. Lu, Engineering the coordination environment of single-atom platinum anchored on graphdiyne for optimizing electrocatalytic hydrogen evolution, *Angew. Chem. Int. Ed.* 57 (2018) 9382–9386, <https://doi.org/10.1002/anie.201804817>.
- [23] L. Zhang, D.-H. Wu, M.U. Haq, J.-J. Feng, F. Yang, A.-J. Wang, Coordination engineering and electronic structure modulation of FeNi dual-single-atoms encapsulated in N, P-codoped 3d hierarchically porous carbon electrocatalyst for synergistically boosting oxygen reduction reaction, *Appl. Catal. B* 351 (2024) 123991, <https://doi.org/10.1016/j.apcatb.2024.123991>.
- [24] L. Dai, Y. Xue, L. Qu, H.-J. Choi, J.-B. Baek, Metal-free catalysts for oxygen reduction reaction, *Chem. Rev.* 115 (2015) 4823–4892, <https://doi.org/10.1021/cr5003563>.
- [25] Y. Li, W. Zhou, H. Wang, L. Xie, Y. Liang, F. Wei, J.-C. Idrobo, S.J. Pennycook, H. Dai, An oxygen reduction electrocatalyst based on carbon nanotube-graphene complexes, *Nat. Nanotechnol.* 7 (2012) 394–400, <https://doi.org/10.1038/nano.2012.72>.
- [26] X. Wang, Y. Jia, X. Mao, D. Liu, W. He, J. Li, J. Liu, X. Yan, J. Chen, L. Song, A. Du, X. Yao, Edge-rich Fe-N₄ active sites in defective carbon for oxygen reduction catalysis, *Adv. Mater.* 32 (2020) 2000966, <https://doi.org/10.1002/adma.202000966>.

[27] M. Xiao, Z. Xing, Z. Jin, C. Liu, J. Ge, J. Zhu, Y. Wang, X. Zhao, Z. Chen, Preferentially engineering FeN₄ edge sites onto graphitic nanosheets for highly active and durable oxygen electrocatalysis in rechargeable Zn-air batteries, *Adv. Mater.* 32 (2020) 2004900, <https://doi.org/10.1002/adma.202004900>.

[28] L. Cui, J. Zhao, G. Liu, Z. Wang, B. Li, L. Zong, Rich edge-hosted single-atomic Cu-N₄ sites for highly efficient oxygen reduction reaction performance, *J. Colloid Interface Sci.* 622 (2022) 209–217, <https://doi.org/10.1016/j.jcis.2022.04.098>.

[29] J. He, N. Wang, Z. Cui, H. Du, L. Fu, C. Huang, Z. Yang, X. Shen, Y. Yi, Z. Tu, Y. Li, Hydrogen substituted graphdiyne as carbon-rich flexible electrode for lithium and sodium ion batteries, *Nat. Commun.* 8 (2017) 1172, <https://doi.org/10.1038/s41467-017-01202-2>.

[30] Q. Lv, W. Si, Z. Yang, N. Wang, Z. Tu, Y. Yi, C. Huang, L. Jiang, M. Zhang, J. He, Y. Long, Nitrogen-doped porous graphdiyne: a highly efficient metal-free electrocatalyst for oxygen reduction reaction, *ACS Appl. Mater. Interfaces* 9 (2017) 29744–29752, <https://doi.org/10.1021/acsmami.7b08115>.

[31] Q. Lv, W. Si, J. He, L. Sun, C. Zhang, N. Wang, Z. Yang, X. Li, X. Wang, W. Deng, Y. Long, C. Huang, Y. Li, Selectively nitrogen-doped carbon materials as superior metal-free catalysts for oxygen reduction, *Nat. Commun.* 9 (2018) 3376, <https://doi.org/10.1038/s41467-018-05878-y>.

[32] Q. Lv, N. Wang, W. Si, Z. Hou, X. Li, X. Wang, F. Zhao, Z. Yang, Y. Zhang, C. Huang, Pyridinic nitrogen exclusively doped carbon materials as efficient oxygen reduction electrocatalysts for Zn-air batteries, *Appl. Catal. B* 261 (2020) 118234, <https://doi.org/10.1016/j.apcatb.2019.118234>.

[33] Y. Zhao, J. Wan, H. Yao, L. Zhang, K. Lin, L. Wang, N. Yang, D. Liu, L. Song, J. Zhu, L. Gu, L. Liu, H. Zhao, Y. Li, D. Wang, Few-layer graphdiyne doped with sp-hybridized nitrogen atoms at acetylenic sites for oxygen reduction electrocatalysis, *Nat. Chem.* 10 (2018) 924–931, <https://doi.org/10.1038/s41557-018-0100-1>.

[34] Y. Zhao, N. Yang, H. Yao, D. Liu, L. Song, J. Zhu, S. Li, L. Gu, K. Lin, D. Wang, Stereodefined codoping of sp-N and S atoms in few-layer graphdiyne for oxygen evolution reaction, *J. Am. Chem. Soc.* 141 (2019) 7240–7244, <https://doi.org/10.1021/jacs.8b13695>.

[35] B. Kang, S. Wu, J. Ma, H. Ai, J.Y. Lee, Synergy of sp-N and sp²-N codoping endows graphdiyne with comparable oxygen reduction reaction performance to Pt, *Nanoscale* 11 (2019) 16599–16605, <https://doi.org/10.1039/C9NR05363H>.

[36] Z. Wang, C. Zhu, H. Tan, J. Liu, L. Xu, Y. Zhang, Y. Liu, X. Zou, Z. Liu, X. Lu, Understanding the synergistic effects of cobalt single atoms and small nanoparticles: enhancing oxygen reduction reaction catalytic activity and stability for zinc-air batteries, *Adv. Funct. Mater.* 31 (2021) 2104735, <https://doi.org/10.1002/adfm.202104735>.

[37] J. Shen, Y. Cai, C. Zhang, W. Wei, C. Chen, L. Liu, K. Yang, Y. Ma, Y. Wang, C.-C. Tseng, J.-H. Fu, X. Dong, J. Li, X.-X. Zhang, L.-J. Li, J. Jiang, I. Pinna, V. Tung, Y. Han, Fast water transport and molecular sieving through ultrathin ordered conjugated-polymer-framework membranes, *Nat. Mater.* 21 (2022) 1183–1190, <https://doi.org/10.1038/s41563-022-01325-y>.

[38] R. Li, M. Zhang, X. Li, X. Ma, C. Huang, Study of graphdiyne-based magnetic materials, *Chem. Res. Chin. Univ.* 37 (2021) 1257–1267, <https://doi.org/10.1007/s40242-021-1350-9>.

[39] X. Li, X. Li, Q. Sun, J. He, Z. Yang, J. Xiao, C. Huang, Synthesis and applications of graphdiyne derivatives, *Acta Phys. Chim. Sin.* 39 (2023) 2206029, <https://doi.org/10.3866/pku.Whx202206029>.

[40] X. Wei, D. Zheng, M. Zhao, H. Chen, X. Fan, B. Gao, L. Gu, Y. Guo, J. Qin, J. Wei, Y. Zhao, G. Zhang, Cross-linked polyphosphazene hollow nanosphere-derived N/P-doped porous carbon with single nonprecious metal atoms for the oxygen reduction reaction, *Angew. Chem. Int. Ed.* 59 (2020) 14639–14646, <https://doi.org/10.1002/anie.202006175>.

[41] X. Wan, Q. Liu, J. Liu, S. Liu, X. Liu, L. Zheng, J. Shang, R. Yu, J. Shui, Iron atom-cluster interactions increase activity and improve durability in Fe-N-C fuel cells, *Nat. Commun.* 13 (2022) 2963, <https://doi.org/10.1038/s41467-022-30702-z>.

[42] M. Li, Q. Lv, W. Si, Z. Hou, C. Huang, Sp-hybridized nitrogen as new anchoring sites of iron single atoms to boost the oxygen reduction reaction, *Angew. Chem. Int. Ed.* 61 (2022) e202208238, <https://doi.org/10.1002/anie.202208238>.

[43] J. Balamurugan, T.T. Nguyen, V. Aravindan, N.H. Kim, J.H. Lee, Highly reversible water splitting cell building from hierarchical 3d nickel manganese oxyphosphide nanosheets, *Nano Energy* 69 (2020) 104432, <https://doi.org/10.1016/j.nanoen.2019.104432>.

[44] J. Balamurugan, P.M. Austeria, J.B. Kim, E.S. Jeong, H.H. Huang, D.H. Kim, N. Koratkar, S.O. Kim, Electrocatalysts for zinc-air batteries featuring single molybdenum atoms in a nitrogen-doped carbon framework, *Adv. Mater.* 35 (2023) 2302625, <https://doi.org/10.1002/adma.202302625>.

[45] J. Balamurugan, T.T. Nguyen, D.H. Kim, N.H. Kim, J.H. Lee, 3D nickel molybdenum oxyselenide (Ni_{1-x}Mo_xOSe) nanoarchitectures as advanced multifunctional catalyst for Zn-air batteries and water splitting, *Appl. Catal. B* 286 (2021) 119909, <https://doi.org/10.1016/j.apcatb.2021.119909>.

[46] J. Balamurugan, T.T. Nguyen, N.H. Kim, D.H. Kim, J.H. Lee, Novel core-shell cumo-oxynitride@n-doped graphene nanohybrid as multifunctional catalysts for rechargeable zinc-air batteries and water splitting, *Nano Energy* 85 (2021) 105987, <https://doi.org/10.1016/j.nanoen.2021.105987>.

[47] Y. Wang, C. Zhang, X. Wang, J. Duan, K. Tong, S. Dai, L. Chu, M. Huang, Engineering carbon-chainmail-shell coated Co₉Se₈ nanoparticles as efficient and durable catalysts in seawater-based Zn-air batteries, *Acta Phys. -Chim. Sin.* 40 (2024) 2305004, <https://doi.org/10.3866/pku.Whx202305004>.

[48] Q. Chang, X. Fu, J. Gao, Z. Zhang, Y. Wang, C. Huang, Y. Li, Electronic reservoir regulation stabilizing IrO_x as efficient cathode for solid-state zinc-air batteries, *CCS Chem.* (2024) 1–14, <https://doi.org/10.31635/ccschem.024.202403989>.